

Modeling winter rainfall in Northwest India using a hidden Markov model: understanding occurrence of different states and their dynamical connections

Indrani Pal · Andrew W. Robertson ·
Upmanu Lall · Mark A. Cane

Received: 24 September 2013 / Accepted: 12 May 2014 / Published online: 23 May 2014
© Springer-Verlag Berlin Heidelberg 2014

Abstract A multiscale-modeling framework for daily rainfall is considered and diagnostic results are presented for an application to the winter season in Northwest India. The daily rainfall process is considered to follow a hidden Markov model (HMM), with the hidden states assumed to be an unknown random function of slowly varying climatic modulation of the winter jet stream and moisture transport dynamics. The data used are from 14 stations over Satluj River basin in winter (December–January–February–March). The period considered is 1977/78–2005/06. The HMM identifies four discrete weather states, which are used to describe daily rainfall variability over study region. Each state was found to be associated with a distinct atmospheric circulation pattern, with the driest and drier states, State 1 and 2 respectively, characterized by a lack of synoptic wave activity. In contrast, the wetter and wettest states, States 3 and 4 respectively, are characterized by a zonally oriented wave train extending across Eurasia between 20N and 40N, identified with ‘western

disturbances’ (WD). The occurrence of State 4 is strongly conditioned by the El Niño and Indian Ocean Dipole (IOD) phenomena in winter, which is demonstrated using large-scale correlation maps based on mean sea level pressure and sea surface temperature. This suggests that there is a tendency of higher frequency of the wet days and intense WD activities in winter during El Niño and positive IOD years. These findings, derived from daily rainfall station records, help clarify the sequence of Northern Hemisphere mid-latitude storms bringing winter rainfall over Northwest India, and their association with potentially predictable low frequency modes on seasonal time scales and longer.

Keywords Winter precipitation · Northwest India · Diagnostics · Western disturbances

1 Introduction

The majority of the meteorological literature on Indian precipitation has focused on the summer monsoon because of its impact on a wider area and greater proportion of the annual total precipitation (Shukla 1975; Washington et al. 1977; Vernekar et al. 1995; Kumar et al. 1999, 2006; Ashok et al. 2001; Gadgil 2003; and many others). The causal structure and predictability of winter precipitation, occurring in the months of December to March, has been relatively less explored due to its limited spatial extent and total amount (Yadav et al. 2010, 2012; Dimri 2013a; Pal et al. 2013a, b). Despite being smaller in amount (about 15–30 % of annual rainfall total; Yadav et al. 2010; Dimri 2013a) and spatial extent as compared to the Indian Summer Monsoon Rainfall (ISM), winter rainfall over the Northwestern states of India, helps reduce the irrigation water demand for winter (rabi) crops (e.g. wheat, barley,

I. Pal (✉)

Department of Civil Engineering, College of Engineering and Applied Science, University of Colorado Denver, 1200 Larimer Street, Campus Box 116, Denver, CO 80204, USA
e-mail: indrani.pal@ucdenver.edu

A. W. Robertson

International Research Institute for Climate and Society (IRI),
The Earth Institute at Columbia University, Palisades,
NY 10964, USA

U. Lall

Department of Earth and Environmental Engineering, Columbia University, New York, NY 10027, USA

M. A. Cane

Lamont-Doherty Earth Observatory, Columbia University,
Palisades, NY 10964, USA

peas, gram and mustard) in this important agricultural region, known as the “Bread Basket” of India. In addition, winter rainfall is accompanied by lower temperatures due to the associated cold advection, which is important for the development of wheat, for example (Yadav et al. 2012). Winter precipitation over the mountainous regions of Northwest India (e.g. Western Himalayas) also helps maintain the winter snowpack and the glaciers, which serve as a vast freshwater storehouse for the important river systems in North India and the rivers originating from the Western Himalayas. The water supply via these rivers to dams and canals is used for power generation and irrigation throughout the year. Winter precipitation over the Western Himalayas falls as rain at lower elevations (approximately <2,000 mASL). An understanding of the winter precipitation dynamics is consequently important in the context of anticipated global climate change that is poorly understood for the Himalayan region.

Winter precipitation over Northwest India and the adjacent Western Himalayas is mainly from eastward-moving synoptic weather systems, known as “western disturbances” (WD) in the form of low-pressure systems traversing Northwestern India (Dimri and Mohanty 2009; Yadav et al. 2012). The associated cyclonic low-level circulations advect warm moist air from the Arabian Sea ahead of the depression, which ascends and contributes to convection, precipitation and the eastward propagation (Yadav et al. 2012). The sun marches to the southern hemisphere during this time of the year, and consequently the whole system of easterly trade and subtropical westerly winds migrate southwards. Over most of Asia, the winds are westerly in the middle and upper troposphere and an intense surface high pressure center, called the “Siberian anticyclone” or “Siberian High” forms over the northern parts of Asia between 40° and 60°N associated with surface cooling (Yadav et al. 2012). The location of the sub-tropical jet during boreal winter is also dictated by the location of the ascending arm of the Hadley cell over the Indian Ocean area adjoining the Maritime continents (Das 1986). Winter precipitation is concentrated in the northern part of the Indian sub-continent in the form of rain in low-lying areas and snowfall at higher altitudes and is generally associated with North–South fluctuations in the position of a 200-hPa subtropical westerly jet (Dimri 2013a). The precipitation has large spatial and temporal variability over this region, with maximum amount of precipitation occurring particularly over the northern mountainous regions in association with WDs, due to the leading role played by orographic convergence and decreasing southwards (Yadav et al. 2012). In the plains, the precipitation decreases from west to east as the WDs lose their strength as they travel eastward.

Among the limited studies that have examined winter precipitation over Northwest India, Rao (1999) analyzed

the relationship between winter precipitation and the Southern Oscillation (SO) index from 1872 to 1993 at the meteorological sub-divisional level. The main findings indicated that there was a significant negative correlation (i.e. the La Niña phase tends to be associated with dryer conditions) for some of the subdivisions in northwestern India. Another major factor found to have a significant determining role on the occurrence of precipitation in India is the surrounding local sea surface temperatures (SSTs of Arabian Sea and Indian Ocean; Sen Roy 2006; Dimri 2013a). Dimri (2013a) examined intra-seasonal oscillations associated with winter precipitation over the Western Himalayas and indicated that intra-seasonal oscillations over this region are mainly driven by moisture convergence and during the peak phase, a strong moisture influx from the Arabian Sea dominates. Dimri (2013b) and Yadav et al. (2010, 2012) studied inter-annual variations of winter precipitation over Western Himalayas and Northwest India respectively, and the in-phase relationship with ENSO forcing. They found that WDs are generally intensified over Northwest India during the warm phase of ENSO. However, the knowledge regarding the timing of WDs, when they contribute to wet or dry days over Northwest India, dynamical structure of WD activities, and their corresponding teleconnections are not well established.

Here we use a hidden Markov model (HMM) to identify different states of winter rainfall on a daily time scale (December–March) over Northwest India, which also indicates the sequence of precipitation events of different magnitude/state brought by the westerly wind. We also determine associations of those states of winter rainfall with daily and seasonal circulation parameters. The rain gauge stations we used here are located in the Satluj River basin, an important water resource for this region. In related previous studies we examined Satluj River flow in spring and monsoon seasons and their diagnostics (Pal et al. 2013a, b) but this study takes a step further to understand WD and associated winter precipitation dynamics in the basin, which also explains the Western Himalayan snow occurrence in winter that contributes to Satluj River flow in the dry spring season.

The paper proceeds as follows. Section 2 describes the datasets and methodology, Sect. 3 describes results and discussion and Sect. 4 summarizes the findings.

2 Data and method

Daily rainfall data for 14 meteorological stations over the Satluj river basin were considered in this study, for the winters 1977/78–2005/06. Figure 1 and Table 1 shows rainfall station location information. The Bhakra Beas Management Board of India provided the data (see

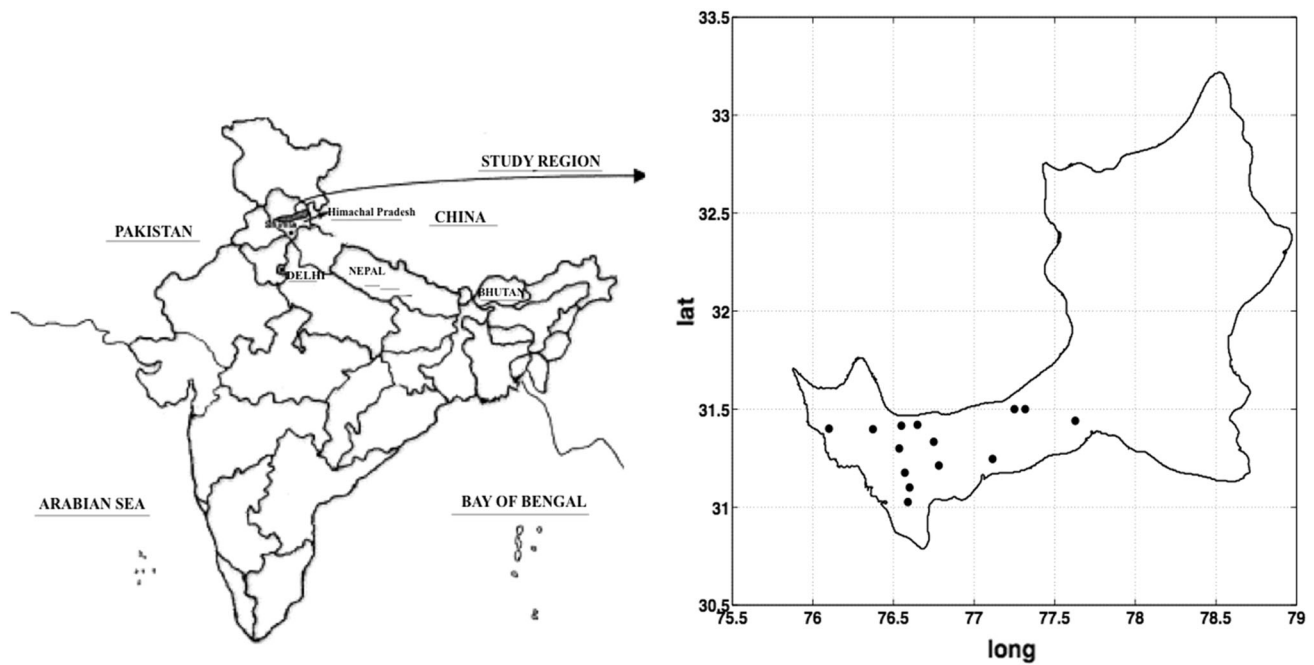


Fig. 1 Satluj River basin in India up to Bhakra reservoir with location of rainfall stations

Table 1 Information of rainfall stations over Satluj River basin in India

No.	Name	Lat (N)	Lon (E)	Elevation (mAMSL)	Occurrence probability	Average intensity on wet days (mm)
1	Berthin	31.42	76.65	668	0.20	9.24
2	Bhartgarh	31.10	76.60	284	0.14	9.36
3	Daslehra	31.42	76.55	562	0.18	10.17
4	Ganguwal	31.40	76.10	1,220	0.15	10.31
5	Ghanauli	31.03	76.59	293	0.13	9.58
6	Kahu	31.21	76.78	526	0.18	9.72
7	Lohand	31.18	76.57	288	0.19	8.86
8	Naina Devi	31.30	76.54	985	0.16	9.23
9	Nangal	31.40	76.37	369	0.15	9.81
10	Rampur	31.44	77.63	987	0.14	10.14
11	Suni	31.25	77.11	701	0.19	8.69
12	Kasol	32.02	77.32	2,614	0.23	8.35
13	Kotla	31.72	77.25	2,824	0.21	9.07
14	Swarghat	31.33	76.75	1,220	0.18	10.68

Acknowledgements). For studying the large-scale atmospheric patterns associated with different rainfall states derived by the HMM, we used National Centers for Environmental Prediction (NCEP)–National Center for Atmospheric Research (NCAR) reanalysis data products (version 1) (Kalnay et al. 1996), obtained from the IRI data library (<http://iridl.ldeo.columbia.edu>). We use December–January–February–March (DJFM) rainfall data for the 14 rain gauge stations. Some researchers define the winter season as DJF (e.g. Dimri 2013a) while some have used DJFM (Yadav et al. 2010). Here we considered DJFM as

the winter season based on the plotted seasonal cycle of precipitation averaged over all the stations (not shown).

The homogeneous HMM was used in order to diagnose different states of winter (DJFM) rainfall over Northwest India. The HMM used here follows the approach of Hughes and Guttorp (1994) to model daily rainfall occurrence, while additionally modeling rainfall amounts (Robertson et al. 2004, 2006). In brief, the time sequence of daily rainfall measurements on a network of stations is assumed to be generated by a first-order Markov chain of a few discrete hidden (i.e. unobserved) rainfall “states”. For each

state, the daily rainfall amount at each station is modeled as a finite mixture of components, consisting of a delta function at zero amount to model dry days, and a combination of two exponentials to describe rainfall amounts on days with nonzero rainfall. The state-transition matrix describes the daily probabilities of transitions between the states. Missing data is treated in the model by deriving the parameter estimates only from the days that are present (Kirshner 2005). The parameters of the model (e.g. all the hidden Markov chain transition probabilities) are estimated from the observed rainfall amount data using the expectation–maximization algorithm (EM), an iterative maximum likelihood method. Details of the HMM and parameter estimation can be found in Robertson et al. (2004, 2006) and Kirshner (2005). Once the values of HMM model parameters have been determined from the rainfall data, the most likely daily sequence of states for the winters 1977/78–2005/06 is estimated using the Viterbi algorithm (Forney 1978). Having thus assigned all the 34×122 days between the different HMM states, composites of meteorological and climatic variables can then be made for each state for diagnostic purposes. Note that while the non-homogeneous form of the HMM can be used for statistical downscaling of rainfall (e.g. Hughes and Guttorp 1994; Robertson et al. 2009), we use it here without predictor variables, purely for diagnostic purposes. The HMM tool was downloaded from the IRI website (<http://iri.columbia.edu/climate/forecast/stochasticTools/index.html#hmm>).

Figure 2 shows values of the Bayesian Information Criterion (BIC), a penalized likelihood measure, obtained from the models with increasing numbers of states. The Bayesian Information Criterion (BIC) is due to Schwarz (1978). It is used to compare a candidate set of statistical

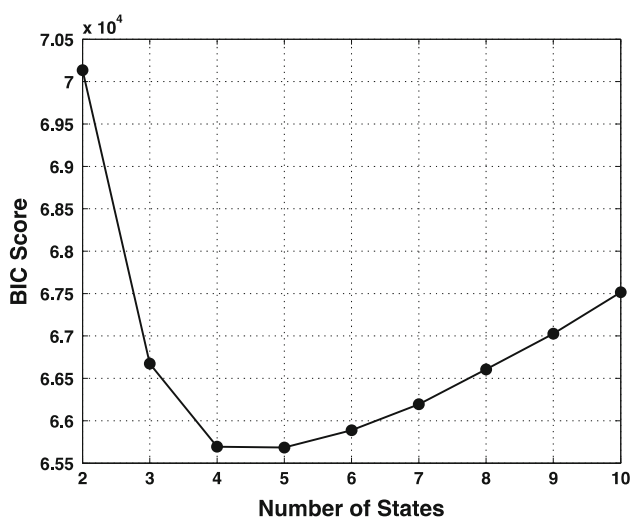


Fig. 2 Number of states in HMM model versus Bayesian Information Criteria (BIC) scores. Based on minimum BIC value, we chose four-state model

models, which may differ in the number of parameters. The uncertainty increases as the number of model parameters increases for a fixed sample size of data. For our applications, different candidate models correspond to different candidate values of hidden states. The total number of parameters includes all the hidden Markov chain transition probabilities. The candidate model that leads to the minimum of the BIC is selected. Figure 2 indicates that selection of four or five state model gives minimum BIC scores. In this study we followed the laws of parsimony and chose a four-state model (Occam’s razor).

3 Results and discussion

Rainfall occurrence probabilities and the corresponding average daily rainfall intensities (mm) on wet days are shown for each state in Fig. 3. The bubbles in the eight-panel figure indicate station locations as well as the magnitudes of occurrence probabilities (top) and daily intensities (bottom). States 1–4 are ordered from driest (State 1) to wettest (State 4) in Fig. 3, in terms of probability of rainfall. Rainfall intensity is relatively low in States 1–3, and very large in State 4. Thus, State 1 represents dry days (near-zero rainfall probability at all stations), States 2 and 3 represent days with low-intensity but more probable rainfall, and State 4 represents days with high probability and high intensity of rain.

The most likely daily sequence of these hidden states over the analysis period 1977/78–2005/06 is plotted in Fig. 4a. One can see that the rainfall is highly intermittent in winter in the study region. The driest state generally dominates over the year, and the wetter-state spells, comprising States 2–4, occur for a few days. The state transition matrix corresponding to Fig. 4a is given in Table 2 (from row to column). Transitions into the wettest states are more often from one of the other wettest states, rather from the dry state; thus, wet spells tend to involve more than one wet state. The number of days/month spent in each state is plotted in Fig. 4b, obtained by averaging the state-occurrences in Fig. 4a column-wise over all years for each calendar month. The frequencies of States 2 and 3 get higher in the month of February and March than the earlier months, while State 1’s frequency decreases from December to March (Fig. 4a, b); thus rainfall generally increases through the season with more-frequent light rain (States 2 and 3) occurring preferentially in the later part of the season, while intense rainfall probability remains constant in January to March at a higher level than in December. Note that the overall frequency of state occurrence decreases quasi monotonically from State 1 to State 4. Interannual variations in state frequency are plotted in Fig. 4c, by summing the state occupancies row-wise in

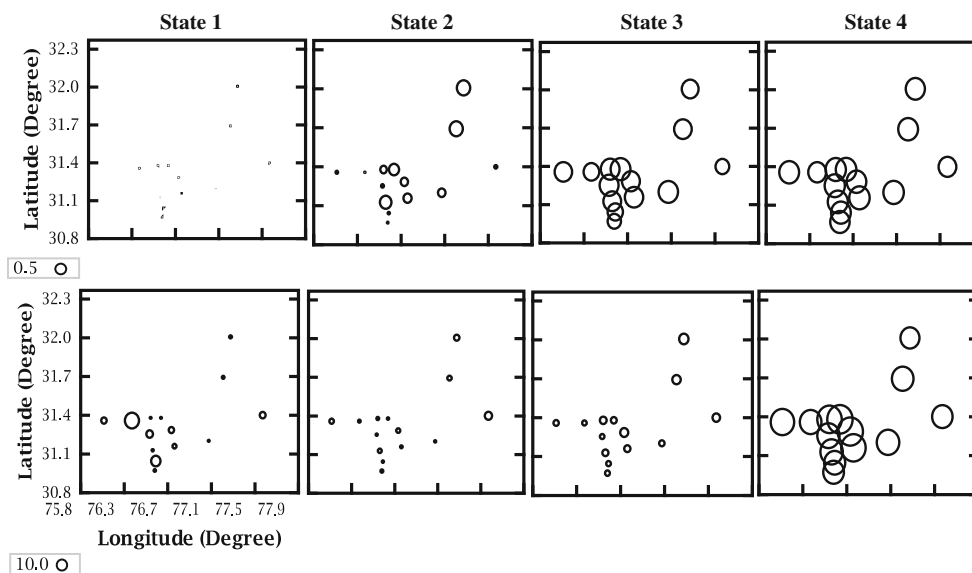


Fig. 3 Occurrence probabilities (*top*) and average daily intensities (mm) for the four-state model. The *bubbles* indicate rainfall station locations and magnitudes

Fig. 4a. A slight upward trend in State 1 and downward in State 3 is visible from 1978 to 2006 in Fig. 4c, though neither trend is statistically significant as per non-parametric Mann–Kendall test.

3.1 Meteorological associations

Here we describe the daily synoptic conditions associated with each state by constructing composite anomaly maps (Figs. 5, 6, 7) of meteorological variables from reanalysis data by averaging all the days that fall into each HMM state in Fig. 4a, and subtracting the climatological DJFM average. We considered geopotential height anomalies at 200, 500 and 850-hPa pressure level, wind vector anomalies at 200–1,000-hPa pressure level, vertical motion anomalies at 200-hPa pressure level, vorticity budget at 200-hPa pressure level, vertically integrated moisture flux from 500 to 1,000-hPa pressure level, evaporation and precipitation difference (E–P) anomalies, mean sea level pressure (MSLP), and SST data.

Figure 5 shows the state-averaged mid-troposphere geopotential height anomaly (500-hPa pressure level, Z500), together with mid-troposphere wind vector anomalies (500-hPa pressure level, UV500). The UV500 fields of States 3 and 4 depict a synoptic-scale wavetrain that closely resembles the Western Disturbance (WD) patterns identified in recent studies (Yadav et al. 2010; and Dimri 2013a, 2013b), consisting of a near-circular cyclonic mid-level circulation centered near (70E, 30N). Circulation patterns for States 3 and 4 look quite similar, with State 4 being more intense, consistent with the station rainfall

parameters for each state in Fig. 3. Thus, corresponding to the different HMM states that are constructed from the station daily rainfall observations, active precipitation of different intensity is usually associated with a trough of different intensity, embedded in zonal wavetrain (Fig. 5). Cyclonic circulation anomalies at 500 hPa in Fig. 5 coincide with negative Z500 anomalies in panels b, c and d, consistent with an equivalent barotropic vertical structure. In the States 2, 3, 4 in ascending wet state order, upper-level southwesterly wind flows towards the Northwest and North India regions. Two similar (troughs) but lower in magnitude regional low pressure systems or cyclones are also observed over the Mediterranean Sea and East China Sea south of Japan associated with the wettest state (State 4), while higher and positive Z500 anomalies (high/ridge) are noticed over Siberia, Western Kazakhstan and Western Mediterranean Sea. This wavetrain is centered near 30N, which coincides with the latitude of the subtropical jet, shown in Fig. 6. The occurrence of the driest state (State 1) coincides with positive Z500 anomalies (high/ridge) over the study region and weak anticyclonic conditions, relative to the climatological mean; since by definition the latter includes the WDs, State 1 may simply be identified with the absence of the WD wavetrain.

As Fig. 5 indicates, the intensity of zonal circulation patterns is associated with the intensity of rainfall corresponding to different states in winter (States 2, 3 and 4 sequentially). Hence we carry out an in depth composite analysis to understand the synoptic meteorological conditions associated with State 4, which enables us to better understand Western Disturbance structure. The vertical

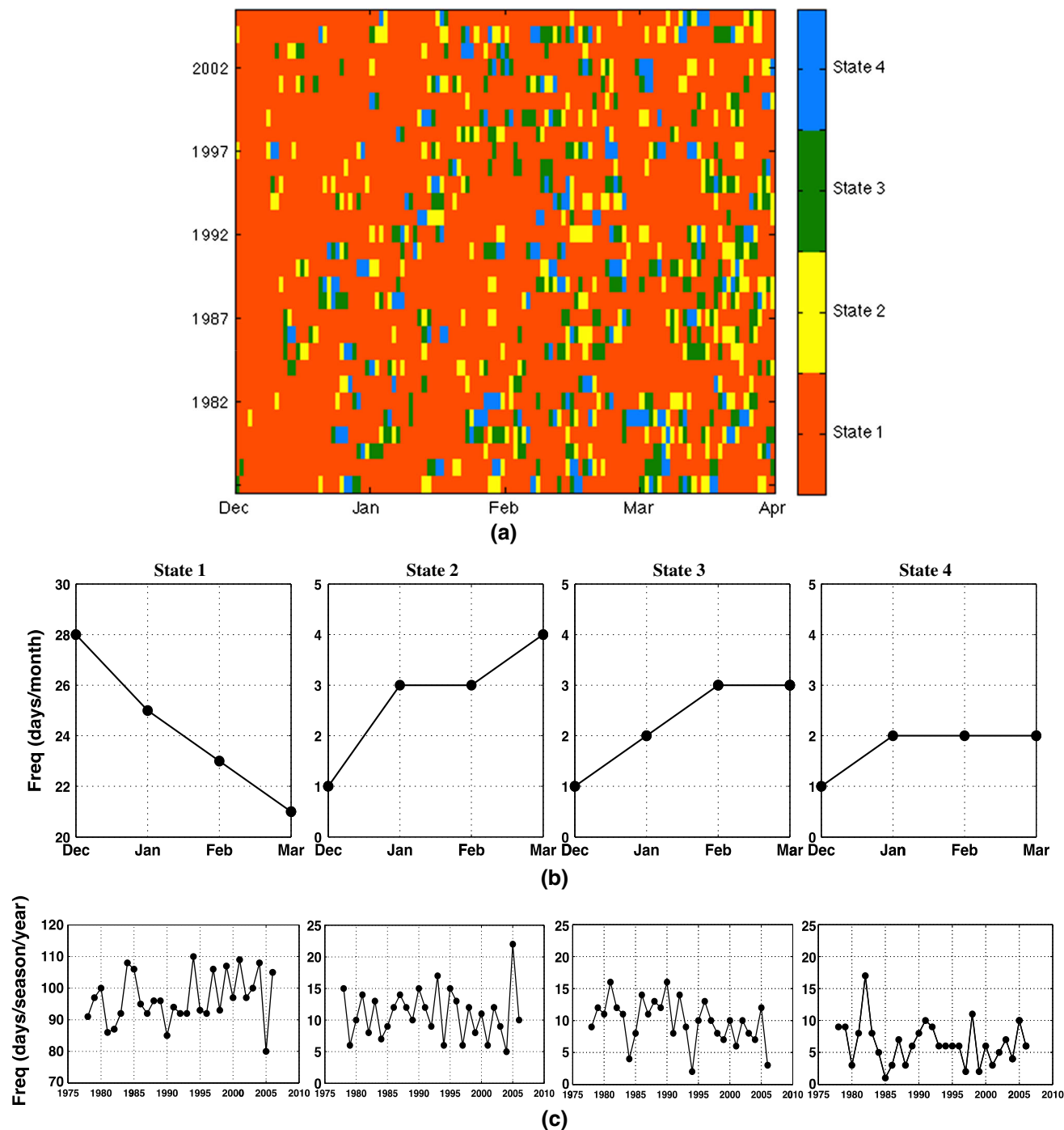


Fig. 4 a Viterbi sequence of most likely states in DJFM from 1978 to 2006; b average monthly states frequency; c seasonal states frequency in each year

structure of the wave associated with State 4 (wettest state) is depicted in Fig. 7 by showing a zoom of the circulation and geopotential height at 200, 500 and 850 hPa. A red square depicts the location of the rainfall stations within Satluj river basin. The wavetrain is pronounced at 200 hPa, i.e. the level of the jet core (Fig. 6, while only the primary center over South Asia is visible at 850 hPa, providing

evidence that the wave is a Rossby wave propagating along the subtropical jet. Very little tilt with height is seen in Fig. 7, indicating that the wave is primarily equivalent barotropic, although a slight westward tilt is seen below 500 hPa. The zonal wavelength is about 60° , or about zonal wavenumber 6, which is nonetheless typical of a baroclinic Rossby wave.

Table 2 Conditional probability matrix

	State 1	State 2	State 3	State 4
State 1	0.880	0.058	0.050	0.012
State 2	0.551	0.197	0.136	0.116
State 3	0.317	0.221	0.245	0.217
State 4	0.264	0.245	0.167	0.324

Figure 8 shows the vertical motion field for State 4 at 200 hPa (colors) along with vectors of UV200, in the larger domain. Here the day 0 field (bottom right) corresponds to zero lag, with composites at negative lag shown in other panels, i.e. with the plotted anomalies leading the rainfall. The vertical motion anomalies are in phase quadrature with the winds, with ascent ahead (i.e. to the east) of the cyclonic center, coinciding with southerly winds, and descent behind it in the northerlies. This configuration suggests that diabatic heating in the moist southerly flow is balanced by ascent. The associated low-level stretching will induce low-level positive vorticity ahead of the surface center, tending to make the wave propagate eastward. However, at upper levels, compression of vortex tubes will generate anticyclonic vorticity ahead of the trough that will counteract the tendency for the strong mean jet (Fig. 6) to advect the perturbation downstream, causing the wave to slow and grow in situ. The eastward phase propagation is clearly seen in Fig. 8 with an approximate phase speed of 5–6 m/s (15° in 3 days).

The dynamics at upper levels are illustrated in Fig. 9 where panels (b–d) show the vorticity budget at 200 hPa for State 4, illustrating the compensation of vortex compression and zonal advection near 75E and a net residual tendency for eastward propagation. A linearization of the vorticity balance (not shown) indicates that advection of the perturbation by the time-mean flow dominates. Figure 9a shows the anomalous isentropic potential vorticity (IPV) on the 330 K surface (near 200 hPa), together with the 200 hPa anomalous winds for State 4. The cyclonic circulation anomaly is accompanied by an IPV maximum whose dynamical impact may be interpreted analogously to the cyclogenetic situation sketched in Hoskins et al. (1985; their Fig. 21). In the present case the cyclonic upper-air IPV anomaly arrives over a pre-existing low-level baroclinic region characterized by large south–north gradients in moist static energy. The ascent and latent heat release will decrease the effective static stability enhancing the penetration of the IPV anomaly toward the surface (Hoskins et al. 1985), leading in turn to larger low-level moisture advection, tending to amplify the perturbation.

In order to explore the energy source of the wave, Fig. 10 shows average vertically integrated moisture flux (from 500 to 1,000-hPa pressure level) as well as the anomalies of the evaporation and precipitation differences (E–P) corresponding to State 4 of DJFM rainfall. Low-level westerly and southwesterly moisture flows towards the Himalayan region forming a convergence zone at

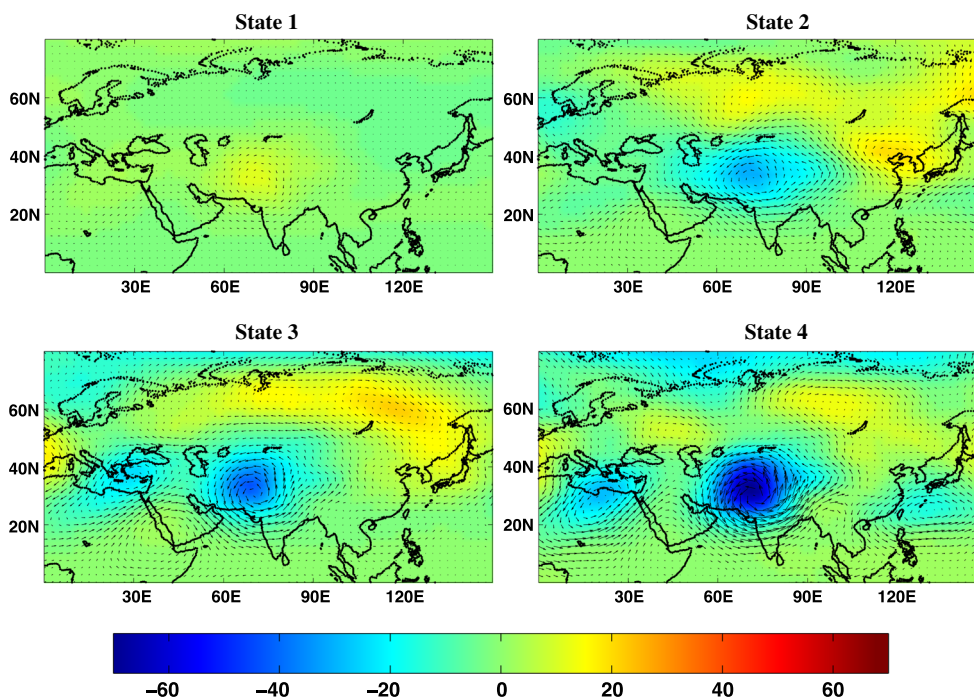


Fig. 5 Average circulation parameter anomalies (Z500 and 500 hPa wind vectors) corresponding to the occurrences of different model states of DJFM rainfall—calculated as the average over the days when a particular rainfall state occurred

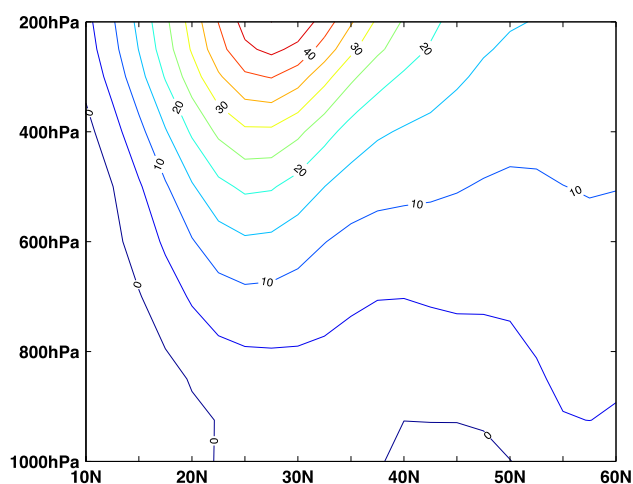


Fig. 6 Latitude-height cross-section of the climatological JFM mean zonal wind associated with State 4 averaged zonally between 30 and 90°W. JFM corresponds to max frequency of State 4

0 days lag from State 4 occurrence. The center of active convection is found over the Himalayan region, corresponding to the center of large moisture flux convergence. This finding to some extent agrees with Dimri (2013a), who reported a strong moisture influx from the Arabian Sea dominating during the peak phase of intra-seasonal oscillation of Western Himalayan winter (DJF) precipitation. Winter Himalayan winter precipitation relates to Northwest India rainfall at the lower elevation during the winter time, as reported in Pal et al. (2013a, b).

3.2 Climatic associations and teleconnections of WD activity

To look at the climatic associations of different state frequencies (shown in Fig. 4c) and teleconnections of WD activities in winter, Pearson correlation coefficients between the state frequencies (number of days/season) and concurrent seasonal (DJFM) MSLP, SST and Z500 anomalies are determined. The results are shown in Figs. 11, 12, 13. The corresponding statistically significant correlated regions (95 %) are also indicated in Figs. 11, 12, 13 by the dotted contours.

The correlation patterns between global MSLP and seasonal frequency of State 1 (driest state) are visibly almost opposite to State 4 (wettest state) over the Eastern Indian Ocean and Western Pacific (Fig. 11). Similarly, the correlation patterns corresponding to State 1 frequency are also opposite in sign to States 2 and 3—the other wet states. A strong dipole pattern of correlation, as observed over the Northeast and Northwest of China in Fig. 11 corresponding to State 1, is minimized for the wetter states (States 2, 3, and 4). In addition, a positive significant correlation pattern over the Northeast of China

corresponding to State 1 differs in sign for that of State 2 over the same region. On the other hand, a strong negative significant correlation pattern over the Northwest of China corresponding to State 3 also differs in sign from the pattern corresponding to State 1 over the same region. In addition, meridional differences in correlation patterns between Indian Ocean and Northern Himalayas, especially on the Northwestern China, is significant for the wet states of 3 and 4. That might be leading to more south–north transport of moisture for the wet states, which could also be important for North–South fluctuation of a upper tropospheric subtropical westerly jet (Dimri 2013a).

It is known that the MSLP conditions over the region of Western Pacific Ocean are also an indicator of SO. The SO accompanies the variation in SST of the tropical Eastern Pacific Ocean (warming and cooling known as El Niño and La Niña, respectively). The warm oceanic phase, El Niño, accompanies high air surface pressure in the Western Pacific, while the cold phase, La Niña, accompanies low air surface pressure over the Western Pacific. The correlation patterns between the frequency of each state and the Western Pacific MSLP indicates that the different rainfall states are associated with concurrent seasonal ENSO conditions. This is also indicated in Fig. 12 for SST anomaly, where we notice a positively significant correlated area over the tropical eastern Pacific Ocean corresponding to the wettest State 4. This indicates that the tele-connections of WD activity seem to be associated to large extent with the type of SST warming over the tropical Pacific or ENSO patterns. Bottom right panel in Fig. 12 indicates that El Niño is associated with intense WDs (State 4), while less intense WDs (State 3) are not related to ENSO. Hence it is apparent that while ENSO changes WD intensity, it does not change WD frequency, which was not reported before. The WD intensity change is due to the fact that ENSO strengthens the subtropical jet over Asia shifting it southwards (Dimri 2013a). The association between state frequency and DJFM-average MSLP gradients over the Himalayas seen in Fig. 11 is consistent with this argument.

Figure 13 shows anomaly correlation between different state frequencies and geopotential height at 500 hPa pressure level (Z500). This figure identifies and documents recurrent spatial patterns during various levels of WD activities causing different states of rainfall, which is indicative of standing oscillations in the planetary waves during Northern Hemisphere winter (DJFM). Figure 13 indicates that various states' frequency is mainly related to atmospheric oscillation patterns over the tropical oceans and Northern Hemispheric land area. For example, because higher number of intense WD activities is related to stronger thermal effect of tropical ocean SSTs, most intense WD activity corresponding to State 4 is related to mid-tropospheric circulation fields of tropical Oceans. In

Fig. 7 Vertical structure of the wave (average circulation parameter anomalies (Z and UV) associated with State 4 (wettest state)

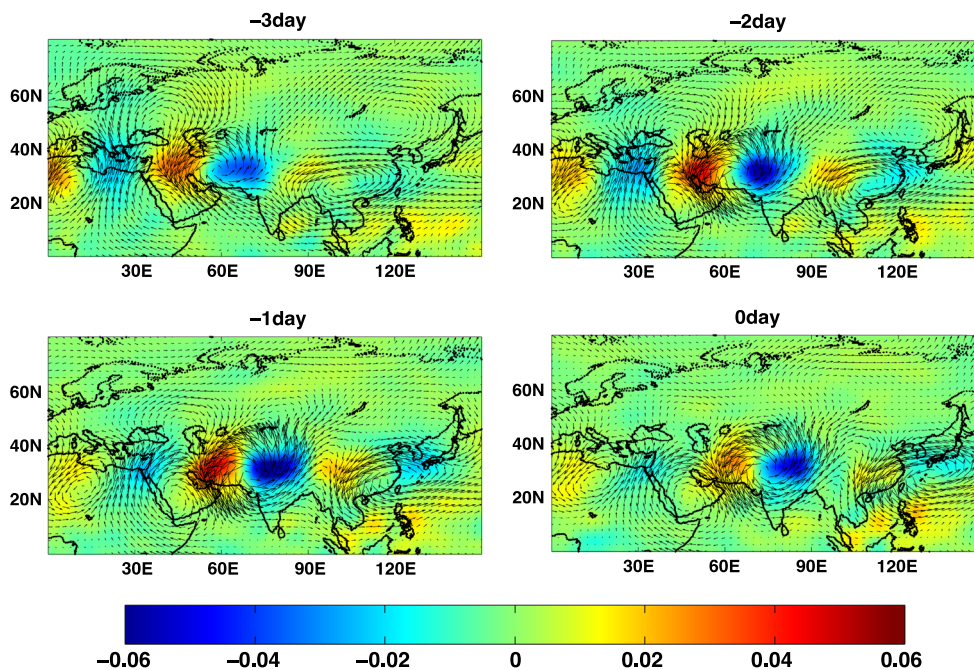
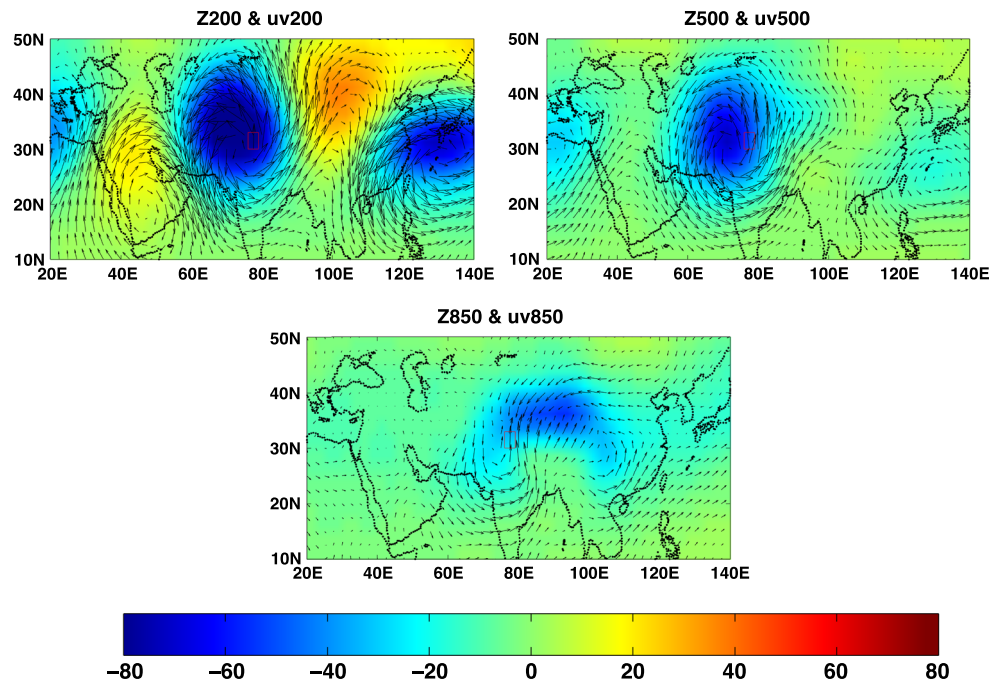


Fig. 8 Concurrent and lagged average circulation parameter anomalies (vvel200 and 200 hPa wind vectors) for State 4

addition, trains of positive and negative correlation patterns are visible in the Northern Hemisphere, which also indicates associations with zonal circulation patterns. For example, a positive significant correlation field is noticed for State 4 over the far west of Northwest India covering the Middle East, in Fig. 13. The differences between circulation patterns for States 1, 2, 3 and 4 occurrences are the strengths between the dipole nature of correlations between

Z500 over Siberia and over North and Northwest India, which enhances for States 3 and 4 as compared to State 2, which is opposite for State 1.

Since seasonal wettest state (State 4) frequency, albeit smaller in number but greater in magnitude, was found to be significantly and positively correlated with the Eastern to Central pacific SST (Fig. 12), and the opposite was true for State 1, we carried out a separate correlation analysis

Fig. 9 Upper level vorticity diagnostics for State 4: **a** isentropic potential vorticity (IPV) anomaly at 330 K (contours 0.1 PVU) and 200 hPa wind anomalies; and **b–d** time tendencies in the vorticity balance at 200 hPa (without the time mean subtracted) due to: **b** horizontal advection, **c** vertical advection (i.e. “stretching”), and **d** the sum of these tendencies. Contour interval in **b–d** is $2 \times 10^{-11} \text{ s}^{-2}$, with warm colors positive. The IPV was constructed from the European Reanalysis (ERA) Interim product (Dee et al. 2011)

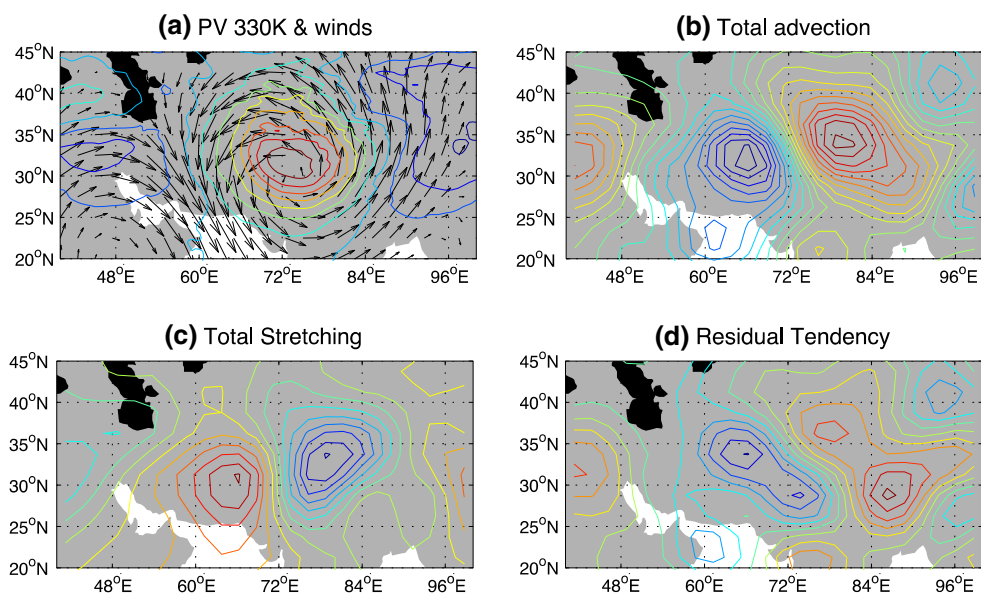
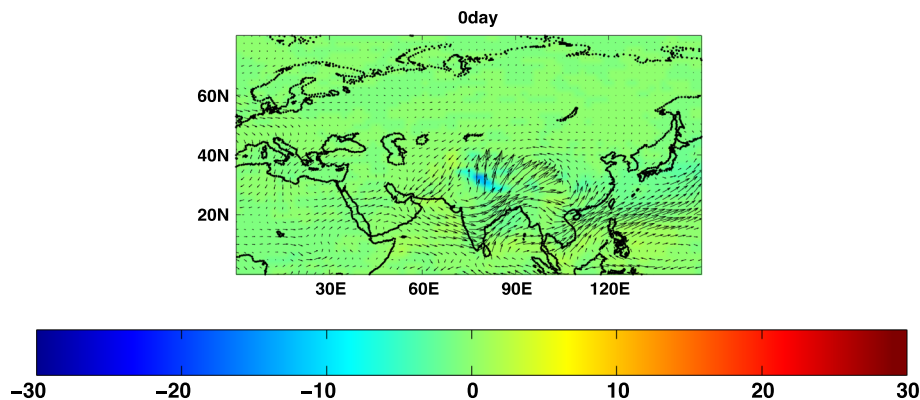


Fig. 10 Concurrent moisture flux and E–P for State 4



between different state frequencies and ENSO indices during concurrent times and also at certain time lags. In addition, since the correlation patterns with MSLP/SST/Z500 over the Indian Ocean were also associated with different states frequency, we also carried out a correlation study between different state frequencies and Indian Ocean Dipole index (IOD). The correlations were determined both for DJFM and the different combinations of the months therein. We found that ENSO indices (SOI, Nino3.4, Nino4, Nino3) are significantly correlated with the seasonal frequency of State 4 and State 2. These associations are also visible in Figs. 11 and 12, meaning that El Niño years tend to be associated with higher number of wettest states and therefore intense WD activities. This finding is to some extent consistent with Rao (1999), who indicated that there was a significant negative correlation between SOI and precipitation for some of the subdivisions in Northwestern India. Yadav et al. (2010) also reported positive significant correlation of average winter precipitation over Northwest India and concurrent ENSO conditions (Nino 3.4 index).

There also exist statistically significant correlations between pre-winter (November) SOI and Nino indices, and DJFM State 1, 2 and 4 frequencies. In addition, IOD was also found significantly correlated with State 4 in different combinations of the winter months.

4 Conclusions

Factors governing the occurrence of winter rainfall in the Himalayas are of considerable interest from a practical water management perspective. The range of topography in Northwest India makes numerical climate modeling at local or larger scales a challenge. However, the topography also lends organization to the larger scale mid-latitude circulation, and hence an identification or classification of the larger scale weather patterns and their antecedent climate conditions that influence moisture transport into the region is of interest. The Homogeneous HMM provides a robust approach for clustering or classifying such states

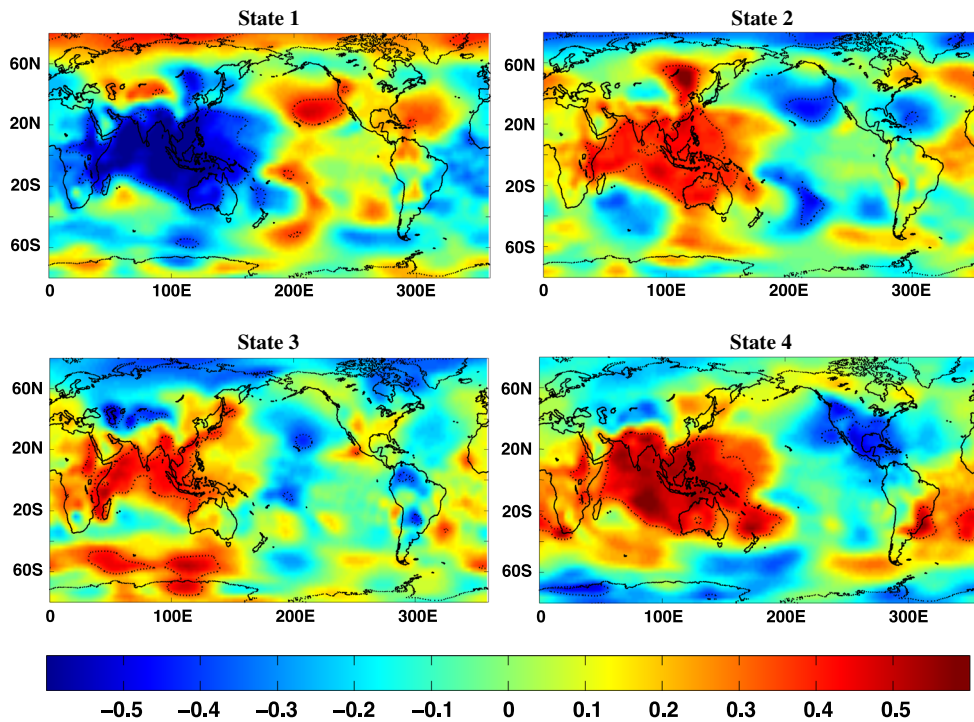
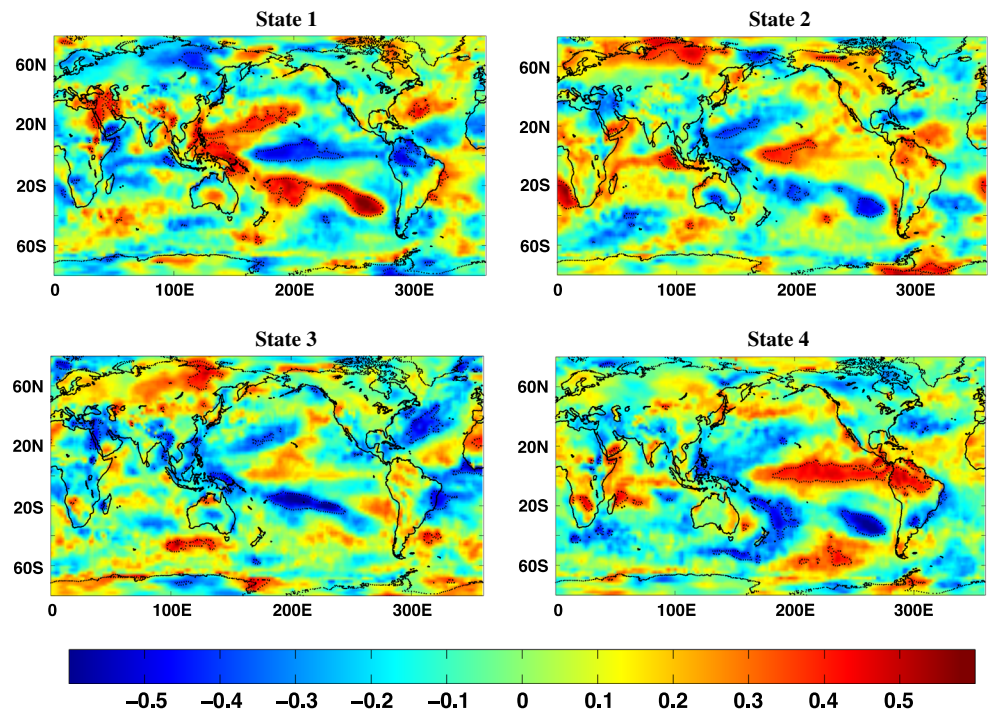


Fig. 11 Pearson correlations between frequencies of different model states of DJFM rainfall (Fig. 4c) and average daily MSLP in DJFM. 95 % significance regions are marked as *dotted contours*

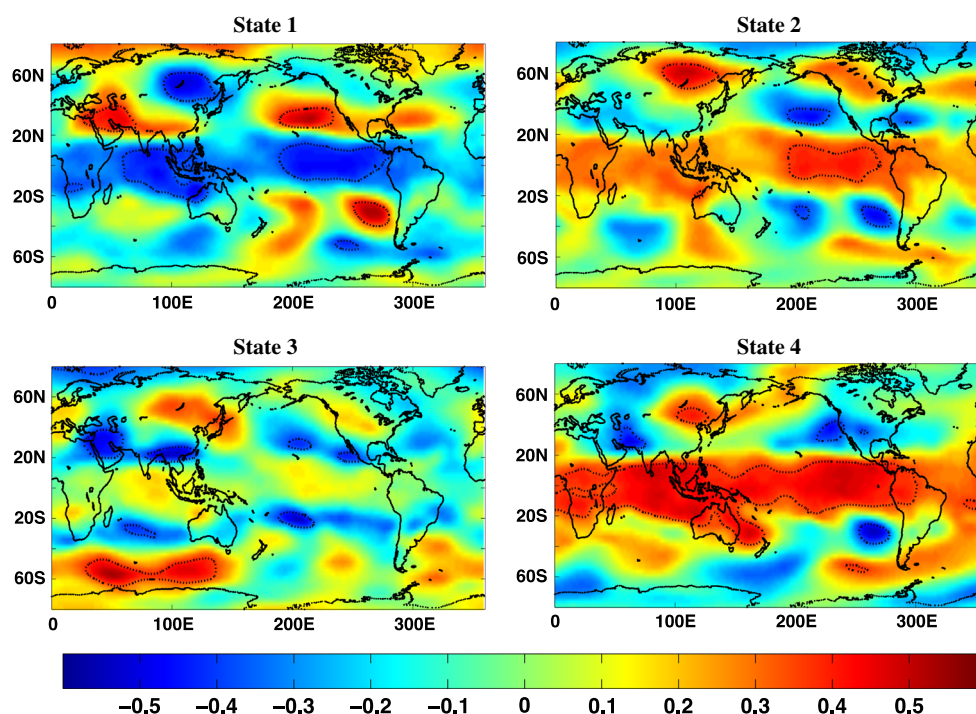
Fig. 12 Pearson correlations between frequencies of different model states of DJFM rainfall (Fig. 4c) and average daily surface temperature in DJFM. 95 % significance regions are marked as *dotted contours*



considering both rainfall heterogeneity in space, and its temporal intermittence characteristics, over the season. The application of the HMM identified four rainfall states categorized by their average daily intensity and occurrence

probability. The wettest states occur with low frequency, but they are highly associated with ENSO and positive IOD conditions. An identification of this association provides a potential nonlinear prediction algorithm.

Fig. 13 Pearson correlations between frequencies of different model states of DJFM rainfall (Fig. 4c) and average daily Z500 in DJFM. 95 % significance regions are marked as *dotted contours*



During the wet rainfall states, convective activities in association with westerly and southwesterly moisture flux were found to be enhanced. Various states of rainfall frequency associated with Western Disturbance intensity were also found associated with SSTs and MSLP variation over the adjacent oceans as well as the tropical Pacific and North and Southern Atlantic. Thus large-scale boundary conditions are shown to map on to the intensity and position of the WDs and hence the likelihood of regional winter precipitation.

Extensions of the work towards understanding the low frequency structure of the variations in these circulation parameters, as well as lead/lag relations with key indicators are in progress, with the goal of building a multi-scale prediction model for winter precipitation and temperature.

Acknowledgments The authors acknowledge Rajeev Bansal, and the Bhakra Beas Management Board of India for sharing the rainfall datasets. AWR was supported by DOE's EaSM Grant DE-SC0006616 and by ONR's MURI Grant N00014-12-1-0911.

References

- Ashok K, Guan Z, Yamagata T (2001) Impact of the Indian Ocean dipole on the relationship between the Indian monsoon rainfall and ENSO. *Geophys Res Lett* 28(23):4499–4502
- Das PK (1986) *Monsoons*. World Meteorological Organization, Fifth WMO lecture, WMO No. 613, Geneva
- Dee DP, Uppala SM, Simmons AJ et al (2011) The ERA-interim reanalysis: configuration and performance of the data assimilation system. *Quat J R Meteorol Soc* 137:553–597. doi:10.1002/qj.828
- Dimri AP (2013a) Intraseasonal oscillation associated with Indian winter monsoon. *J Geophys Res Atmos* 118:1–10. doi:10.1002/jgrd.50144
- Dimri AP (2013b) Interannual variability of Indian winter monsoon over the Western Himalayas. *Global Planet Change* 106:35–50. doi:10.1016/j.gloplacha.2013.03.002
- Dimri AP, Mohanty UC (2009) Simulation of mesoscale features associated with intense western disturbances over western Himalayas. *Meteorol Appl* 16:289–308
- Forney GD Jr (1978) The Viterbi algorithm. In: *Proceedings of the IEEE*, pp 267–278
- Gadgil S (2003) The Indian monsoon and its variability. *Annu Rev Earth Planet Sci* 31(1):429–467
- Hoskins BJ, McIntyre ME, Robertson AW (1985) On the use and significance of isentropic potential vorticity maps. *Quat J R Meteorol Soc* 111:877–946
- Hughes JP, Guttorp P (1994) A class of stochastic models for relating synoptic atmospheric patterns to local hydrologic phenomenon. *Water Resour Res* 30:1535–1546
- Kalnay EM, Kanamitsu R, Kistler W et al (1996) The NCEP/NCAR 40-year reanalysis project. *Bull Am Meteorol Soc* 77(3):437–471
- Kirshner S (2005) Modeling of multivariate time series using hidden Markov models, PhD Thesis, Columbia University
- Kumar KK, Rajagopalan B, Cane MA (1999) On the weakening relationship between the Indian monsoon and ENSO. *Science* 284(5423):2156–2159
- Kumar KK, Rajagopalan B, Hoerling M, Bates G, Cane M (2006) Unraveling the mystery of Indian monsoon failure during El Niño. *Science* 314(5796):115–119
- Pal I, Lall U, Robertson AW, Cane MA, Bansal R (2013a) Predictability of Western Himalayan river flow: melt seasonal inflow into Bhakra reservoir in Northern India. *Hydrol Earth Syst Sci* 17:2131–2146. doi:10.5194/hess-17-2131-2013
- Pal I, Lall U, Robertson AW, Cane MA, Bansal R (2013b) Diagnostics of Western Himalayan Satluj river flow: warm season (MAM/JJAS) inflow into Bhakra dam in India. *J Hydrol* 478:132–147

- Rao GN (1999) Variations of the SO relationship with summer and winter monsoon rainfall over India: 1872–1993. *J Clim* 12:3486–3495
- Robertson AW, Kirshner S, Smyth P (2004) Downscaling of daily rainfall occurrence over Northeast Brazil using a Hidden Markov Model. *J Clim* 17:4407–4424
- Robertson AW, Kirshner S, Smyth P, Charles SP, Bates BC (2006) Subseasonal-to-interdecadal variability of the Australian monsoon over North Queensland. *Quat J R Meteorol Soc* 132:519–542
- Robertson AW, Moron V, Swarimoto Y (2009) Seasonal predictability of daily rainfall statistics over Indramayu district, Indonesia. *Int J Climatol* 29:1449–1462
- Schwarz GE (1978) Estimating the dimension of a model. *Ann Stat* 6(2):461–464. doi:[10.1214/aos/1176344136](https://doi.org/10.1214/aos/1176344136). MR 468014
- Sen Roy S (2006) The impacts of ENSO, PDO, and Local SSTs on winter precipitation in India. *Phys Geogr* 27(5):464–474
- Shukla J (1975) Effect of Arabian Sea surface temperature anomaly on Indian summer monsoon: a numerical experiment with GFDL model. *J Atmos Sci* 32:503–511
- Vernekar AD, Zhou J, Shukla J (1995) The effect of Eurasian snow cover on the Indian monsoon. *J Clim* 8(2):248–266
- Washington W, Chervin R, Rao GV (1977) Effects of a variety of Indian Ocean surface temperature anomaly patterns on the summer monsoon circulation: experiments with the NCAR GCM. *Pure Appl Geophys* 115:1335–1356
- Yadav RK, Yoo JH, Kucharski F, Abid MA (2010) Why is ENSO influencing northwest India winter precipitation in recent decades? *J Clim* 23:1979–1993
- Yadav RK, Rupa Kumar K, Rajeevan M (2012) Characteristic features of winter precipitation and its variability over northwest India. *J Earth Syst Sci* 121(3):6111–6623